AIAA JOURNAL
Vol. 34, No. 9, September 1996

Multidomain Modeling and Analysis of Delaminated Stiffened Composite Shells

B. P. Naganarayana,* B. Z. Huang,† and S. N. Atluri‡
Georgia Institute of Technology, Atlanta, Georgia 30332-0356

A unified method is presented for modeling delaminated stiffened laminated composite shells, synthesizing accurate multiple postbuckling solution paths under compressive loading, and predicting delamination growth. A multidomain modeling technique is presented for modeling the delaminated stiffened shell structures. Error-free formulations are presented for a two-noded curved stiffener element and a three-noded shell element for geometrically nonlinear applications. An accurate and simple automated solution strategy based on Newton-type iterations is presented for predicting the general geometrically nonlinear and postbuckling behavior of structures. Finally, a simple method is derived for predicting the delamination growth by using the pointwise energy release rate at the delamination front as evaluated from the three-dimensional *J* integral.

I. Introduction

LAMINATED composites are gaining importance in aircraft structural applications as a result of their very high strength-to-weight ratios. These applications are, however, still very limited because of the lack of a thorough understanding of the failure mechanisms involved in the laminated structures. In particular, the phenomenon of progressive failure in laminated composite structures is yet to be understood and, as a result, reliable strategies for designing optimal laminated composite structures for desired life and strength are not yet available.

It is known that delaminations are the most frequent causes of failure of laminated structures, particularly under compressive loads. The presence of delaminations leads to a reduction in the overall buckling strength of the structure. In addition, the delaminations tend to grow rapidly under postbuckling loads, causing further reduction in structural strength and leading ultimately to fatal structural failure. Very limited analytical work in this area exists in the literature.[1,2]

In this paper, in an effort to gain understanding of the strength reduction resulting from the presence of delaminations and the mechanisms of delamination growth, a unified method is developed for modeling delaminated stiffened composite structures, for accurately predicting their geometrically nonlinear behavior under normal and postbuckling loading conditions, and for predicting delamination growth by using the pointwise energy release rate at the delamination front.

The transverse shear deformation is found to play an important role in cases of laminated composite structures. Hence, the transverse shear deformation of the structure is explicitly introduced in this work in accordance with the Reissner–Mindlin theory of shell flexure. The junction between the delaminated sublaminates and the nondelaminated shell is modeled by using a two-dimensional generalization of the so-called multidomain model[3] presented earlier for one-dimensional problems by Chai et al.[4] The stiffener degrees of freedom are related to the shell degrees of freedom, again, in accordance with the Reissner–Mindlin theory.

A two-noded curved stiffener element (BEAM2)[5] and a three-noded shell element (SHELL3)[6] are developed based on the respective theoretical formulations. In the case of the shell element, the C^0 continuity is exactly preserved for the field variables. However, the C^1 continuity required for the transverse deflection across the element boundaries is achieved a posteriori in a weak form. The causes of locking and the associated stress oscillations are located. The constrained strain fields are modified to eliminate locking using appropriate reduced integration for the associated constrained components of the strain energy.

An automated, incremental, general nonlinear and postbuckling Newton-type solution strategy, incorporating an arc length–controlled load incrementation and branch switching based on a linearized asymptotic solution,[7,8] is utilized while using the displacement-type finite element model. The stresses are postprocessed for each load increment, to obtain pointwise energy release rate distribution along the delamination front, by using the adapted J-integral approach.[3]

II. Multidomain Model

In this paper, we shall consider a general stiffened laminated composite shell with a single delamination of an arbitrary shape and location, subjected to arbitrary compressive loads (Fig. 1). The structure is modeled using the multishell model in which the delaminated shell is assumed to be assembled with three distinct shells: 1) laminate: nondelaminated zone $\Omega^{(1)}$, 2) delaminate: thinner side of the delaminated zone $\Omega^{(2)}$, and 3) base: thicker side of the delaminated zone $\Omega^{(3)}$. The three shells $\Omega^{(i)}$, $i = 1, 2, 3$, respectively, have midsurface areas $\mathcal{A}^{(i)}$, thicknesses $t^{(i)}$, boundaries $\partial\Omega^{(i)}$, and midsurface boundaries $\partial\mathcal{A}^{(i)}$. The delamination edge is denoted by Γ. The assumptions of Reissner–Mindlin theory of plate bending are used for modeling each shell and the joint between them. Thus, for each shell, the three-dimensional displacement field ($\boldsymbol{U} \equiv \{U_1\ U_2\ U_3\}$) can be expressed in terms of the corresponding midsurface displacement ($\boldsymbol{u} \equiv \{u_1\ u_2\ u_3\}$) and rotation ($\boldsymbol{\theta} \equiv \{\theta_1\ \theta_2\ 0\}$) fields as

$$\boldsymbol{U}^{(i)}(x_\alpha, x_3) = \boldsymbol{u}^{(i)}(x_\alpha) - x_3^{(i)}\boldsymbol{\theta}^{(i)}(x_\alpha) \tag{1}$$

where $x_\alpha^{(i)}$ ($\alpha = 1, 2$) are the in-plane curvilinear shell coordinates and $x_3^{(i)}$ is the thickness coordinate for the ith ($i = 1, 2, 3$) shell (Fig. 1). The structural continuity at the delamination front Γ is maintained by assuming the deformation to be unique at the junction of the three shells, i.e., $\boldsymbol{U}^{(1)} = \boldsymbol{U}^{(2)} = \boldsymbol{U}^{(3)}$ on Γ in accordance with the Reissner–Mindlin law of flexure [Eq. (1)]. In other words, at the delamination edge, the midsurface degrees of freedom of the delaminate and the base shells are assumed to be related to those of the nondelaminated shell by

$$\left.\begin{pmatrix} u_3^{(1)} = u_3^{(2)} = u_3^{(3)} \\ \theta_\alpha^{(1)} = \theta_\alpha^{(2)} = \theta_\alpha^{(3)} \\ u_\alpha^{(i)} = u_\alpha^{(1)} + h^{(i)}\theta_\alpha^{(1)} \end{pmatrix}\right|_{\text{at}\,\Gamma} \tag{2}$$

Received April 4, 1995; revision received Oct. 4, 1995; accepted for publication Oct. 6, 1995.

*Visiting Scientist, Computational Modeling Center; on leave from National Aerospace Laboratories, Bangalore 560017, India. Senior Member AIAA.

†Visiting Professor, Computational Modeling Center; on leave from Northeastern University, Liaoning, People's Republic of China.

‡Institute Professor and Regents' Professor of Engineering, Computational Modeling Center. Fellow AIAA.

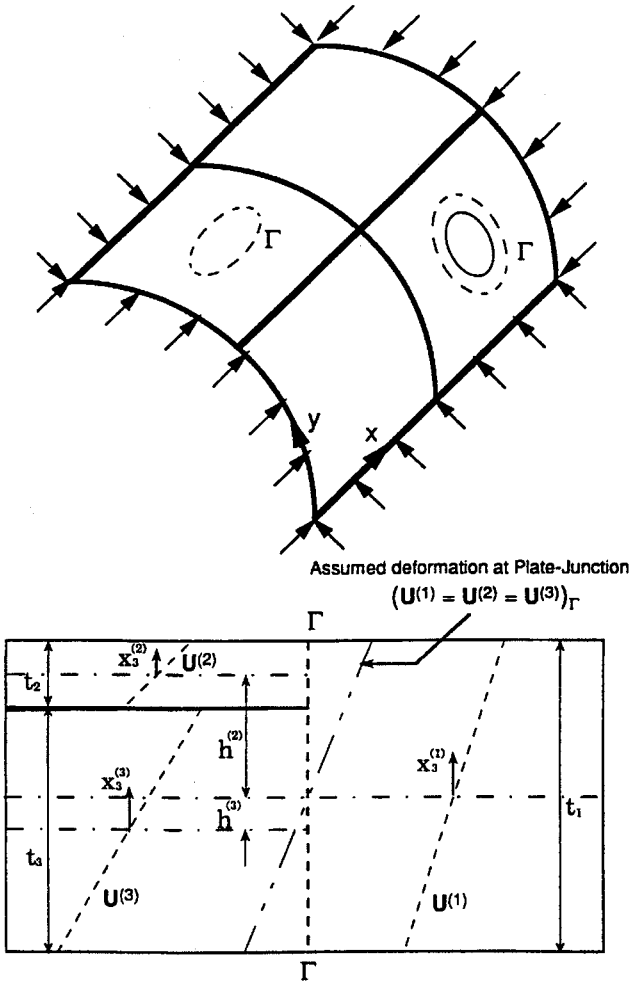

Fig. 1 Multidomain model for delaminated stiffened composite shells.

where $h^{(i)}$ is the distance of the midsurface of the ith shell from the laminate midsurface (Fig. 1). It can be noted that the foregoing continuity conditions at the delamination edge can be modified appropriately when using any other alternative plate/shell theory (e.g., higher-order shear deformable theory) or by choosing appropriate heuristic multipoint constraints based on experience.

Similarly, the beam (stiffener) degrees of freedom are related to the shell degrees of freedom such that the transverse variations of deformation across the shell and beam section are consistent with Reissner–Mindlin theory:

$$u_3^b = u_3^s, \qquad \theta_\alpha^b = \theta_\alpha^s, \qquad u_\alpha^b = u_\alpha^s + e\theta_\alpha^s \tag{3}$$

where superscripts b and s represent beam and shell degrees of freedom, respectively, and e is the eccentricity of the stiffener's neutral axis with reference to the neutral surface of the shell.

If ϕ_α ($\alpha = 1, 2$) are the midsurface rotations characterizing the transformation of the normal to the undeformed midsurface to that of the deformed midsurface, we have

$$\phi_\alpha = u_{3,\alpha} + b_{\alpha\beta}u_\beta \tag{4}$$

where $\boldsymbol{b}$ is the curvature tensor of the shell's midsurface.

In the present formulation, the engineering transverse shear strains $\gamma_{\alpha 3}$ are considered as independent midsurface degrees of freedom, assuming that they do not vary over the shell thickness. The engineering transverse shear strains are related to the section rotations θ_α and the midsurface rotations ϕ_α in accordance with the Reissner–Mindlin theory of plate flexure as

$$\gamma_{\alpha 3} = \phi_\alpha - \theta_\alpha \tag{5}$$

For each shell, the in-plane strain components ($\epsilon_{11}, \epsilon_{22}, \epsilon_{12}$) and the transverse shear strain components ($\epsilon_{13}, \epsilon_{23}$) of the three-dimensional Green–Lagrange strain tensor (including large deformations) are given by

$$\epsilon_{\alpha\beta}^{(i)} = \tfrac{1}{2}[U_{\alpha,\beta} + U_{\beta,\alpha} + (U_{3,\alpha} + b_{\alpha\beta}U_\beta) \times (U_{3,\beta} + b_{\beta\alpha}U_\alpha) - b_{\alpha\beta}U_3]^{(i)}$$
$$\epsilon_{\alpha 3}^{(i)} = \tfrac{1}{2}[\gamma_{\alpha 3}]^{(i)} \tag{6}$$

respectively, where, again, $\alpha, \beta = 1, 2$ and $i = 1, 2, 3$. Using the three-dimensional displacement field description [Eq. (1)] in Eqs. (6) and neglecting the nonlinear terms associated with the section rotations, the in-plane components of the Green–Lagrange strain tensor can be simplified as

$$\epsilon_{\alpha\beta}^{(i)} = \left(\varepsilon_{\alpha\beta l}^{(i)} + \nu_{\alpha\beta}^{(i)}\right) + x_3^{(i)}\left(\kappa_{\alpha\beta}^{(i)} + \chi_{\alpha\beta}^{(i)}\right) \tag{7}$$

where $\varepsilon_{\alpha\beta l}^{(i)}$ and $\nu_{\alpha\beta}^{(i)}$ are the linear and nonlinear components of the membrane strains and $\kappa_{\alpha\beta}^{(i)}$ and $\chi_{\alpha\beta}^{(i)}$ are the flexural strain components related to midsurface rotations ϕ_α and transverse shear strains $\gamma_{\alpha 3}$, respectively, given by

$$\begin{aligned}
\varepsilon_{\alpha\beta l}^{(i)} &= \tfrac{1}{2}[u_{\alpha,\beta} + u_{\beta,\alpha}]^{(i)} - [b_{\alpha\beta}u_3]^{(i)} \\
\nu_{\alpha\beta}^{(i)} &= \tfrac{1}{2}[(u_{3,\alpha} + b_{\alpha\beta}u_\beta)(u_{3,\beta} + b_{\beta\alpha}u_\alpha)]^{(i)} \\
\kappa_{\alpha\beta}^{(i)} &= -\tfrac{1}{2}[(u_{3,\alpha} + b_{\alpha\beta}u_\beta)_{,\beta} + (u_{3,\beta} + b_{\beta\alpha}u_\alpha)_{,\alpha}]^{(i)} \\
\chi_{\alpha\beta}^{(i)} &= \tfrac{1}{2}[\gamma_{\alpha 3,\beta} + \gamma_{\beta 3,\alpha}]^{(i)}
\end{aligned} \tag{8}$$

Equation (7) can be written in a compact form to express the three-dimensional Green–Lagrange strain components $\epsilon^{(i)} = \{\epsilon_{11}\ \epsilon_{22}\ \epsilon_{12}\ \epsilon_{13}\ \epsilon_{23}\}^{(i)}$ in terms of the two-dimensional strain components $\epsilon^{(i)} = \{\epsilon_{11}\ \epsilon_{22}\ \epsilon_{12}\}^{(i)}$, $\boldsymbol{\nu}^{(i)} = \{\nu_{11}\ \nu_{22}\ \nu_{12}\}^{(i)}$, $\boldsymbol{\kappa}^{(i)} = \{\kappa_{11}\ \kappa_{22}\ \kappa_{12}\}^{(i)}$, $\boldsymbol{\chi}^{(i)} = \{\chi_{11}\ \chi_{22}\ \chi_{12}\}^{(i)}$, and $\boldsymbol{\gamma}^{(i)} = \{\gamma_{13}\ \gamma_{23}\}^{(i)}$ as

$$\epsilon^{(i)} = \begin{Bmatrix} (\boldsymbol{\varepsilon}_l + \boldsymbol{\nu}) + x_3(\boldsymbol{\kappa} + \boldsymbol{\chi}) \\ \tfrac{1}{2}\boldsymbol{\gamma} \end{Bmatrix}^{(i)} = \boldsymbol{B} \cdot \boldsymbol{\delta} \tag{9}$$

where $\boldsymbol{\delta} = \{u_1\ u_2\ u_3\ u_{3,1}\ u_{3,2}\ \gamma_{13}\ \gamma_{23}\}$ is the vector of independent degrees of freedom and $\boldsymbol{B}$ the strain-displacement matrix.

Assuming orthotropic material behavior for each lamina, the in-plane stresses $\boldsymbol{\sigma}^{(i)} = \{\sigma_{11}\ \sigma_{22}\ \sigma_{12}\}^{(i)}$ and the transverse shear stresses $\boldsymbol{\tau}^{(i)} = \{\tau_{13}\ \tau_{23}\}^{(i)}$ are related to the corresponding strain components as

$$\begin{Bmatrix} \boldsymbol{\sigma} \\ \boldsymbol{\tau} \end{Bmatrix}^{(i)} = \begin{bmatrix} E_{11} & E_{12} & E_{16} & 0 & 0 \\ E_{12} & E_{22} & E_{26} & 0 & 0 \\ E_{16} & E_{26} & E_{66} & 0 & 0 \\ 0 & 0 & 0 & E_{44} & E_{45} \\ 0 & 0 & 0 & E_{45} & E_{55} \end{bmatrix}^{(i)} \times \begin{Bmatrix} (\boldsymbol{\varepsilon}_l + \boldsymbol{\nu}) + x_3(\boldsymbol{\kappa} + \boldsymbol{\chi}) \\ \tfrac{1}{2}\boldsymbol{\gamma} \end{Bmatrix}^{(i)} \tag{10}$$

where the material constitutive terms $E_{ij}^{(i)}$ are functions of the thickness coordinate of each shell $x_3^{(i)}$. Generally, for a laminate with orthotropic layers, $E_{ij}^{(i)}$ are assumed to be piecewise constants over the laminate thickness.

Now, for each shell, the strain energy density (per unit volume) can be calculated using Eqs. (9) and (10) as

$$W^{(i)} = \{\boldsymbol{\sigma} \cdot [(\boldsymbol{\varepsilon}_l + \boldsymbol{\nu}) + x_3(\boldsymbol{\kappa} + \boldsymbol{\chi})]\}^{(i)} + [\boldsymbol{\tau} \cdot \boldsymbol{\gamma}]^{(i)} \tag{11}$$

As we can observe from Eqs. (7–10), the strain field is a linear function in x_3, whereas the stress field is a piecewise linear function in x_3. Hence, it is often more useful to integrate the strain energy density explicitly in the thickness direction and define strain energy density per unit area as

$$\hat{W}^{(i)} = \int_{t_i} W^{(i)}\, dx_3 = [\boldsymbol{N} \cdot (\boldsymbol{\varepsilon}_l + \boldsymbol{\nu}) + \boldsymbol{M} \cdot (\boldsymbol{\kappa} + \boldsymbol{\chi}) + \boldsymbol{Q} \cdot \boldsymbol{\gamma}]^{(i)} \tag{12}$$

where $N \equiv \{N_{11}\ N_{22}\ N_{12}\}$ are the in-plane stress resultants, $M \equiv \{M_{11}\ M_{22}\ M_{12}\}$ are the bending moment resultants, and $Q \equiv \{Q_{13}\ Q_{23}\}$ are the transverse shear stress resultants given for each shell by

$$\begin{Bmatrix} N \\ M \\ Q \end{Bmatrix}^{(i)} = \begin{bmatrix} A & B & 0 \\ B & D & 0 \\ 0 & 0 & G \end{bmatrix}^{(i)} \begin{Bmatrix} (\varepsilon_l + \nu) \\ (\kappa + \chi) \\ \gamma \end{Bmatrix}^{(i)} \tag{13}$$

and

$$(A_{kl}, B_{kl}, D_{kl})^{(i)} = \int_{t_i} E_{ij}^{(i)}(x_3)\left(1, x_3, x_3^2\right) dx_3$$

$$G_{mn}^{(i)} = \int_{t_i} s_m s_n E_{ij}^{(i)}(x_3)\, dx_3$$

as $k, l = 1, 2, 3$ correspond to $i, j = 1, 2, 6$ and $m, n = 1, 2$ correspond to $i, j = 4, 5$; s_1 and s_2 are the shear correction factors in the transverse planes 1–3 and 2–3, respectively. Integrating $\hat{W}^{(i)}$ [Eq. (13)] over the shell domains, we get the total strain energy stored in the ith shell as

$$\bar{W}^{(i)} = \frac{1}{2}\int_{\mathcal{A}^{(i)}} \hat{W}^{(i)}\, d\mathcal{A}$$

$$= \int_{\mathcal{A}^{(i)}} \frac{1}{2}[N \cdot (\varepsilon_l + \nu) + M \cdot (\kappa + \chi) + Q \cdot \gamma]^{(i)}\, d\mathcal{A} \tag{14}$$

If $f^{(i)} = \{f_1\ f_2\ f_3\}^{(i)}$ are the body force components acting on the ith shell and $F = \{F_1\ F_2\ F_3\}^{(i)}$ are the traction forces acting on the boundaries of the ith shell, all defined in the curvilinear shell coordinate system, the potential of the external forces on the ith shell is given by

$$P^{(i)} = \int_{\Omega^{(i)}} f \cdot U\, d\Omega + \int_{\partial\Omega^{(i)}} F \cdot U\, d\mathcal{A} \tag{15}$$

Assuming that the body force components and the transverse traction force component do not vary over shell thickness and that in-plane traction force components vary linearly over the thickness, we get

$$P^{(i)} = \int_{\mathcal{A}^{(i)}} (\hat{f} \cdot u)^{(i)}\, d\mathcal{A} + \int_{\partial\mathcal{A}^{(i)}} (\hat{F} \cdot u + \hat{M} \cdot \theta)^{(i)}\, d\Gamma \tag{16}$$

where

$$\hat{f}^{(i)} = \int_{t_i} f^{(i)}\, dx_3, \qquad \hat{F}^{(i)} = \int_{t_i} F^{(i)}\, dx_3$$

$$\hat{M}^{(i)} = \int_{t_i} F^{(i)} x_3\, dx_3$$

and $\hat{M}^{(i)} = \{\hat{M}_1\ \hat{M}_2\ 0\}^{(i)}$ represent the traction moments acting on $\partial\mathcal{A}^{(i)}$.

Then, using Eqs. (14) and (15), we find that the total potential energy for the assembly of shells is given by

$$\Pi = \sum_{i=1}^{3} \left(\bar{W}^{(i)} - P^{(i)}\right) \tag{17}$$

Applying the minimum total potential energy principle ($\delta\Pi = 0$), we obtain the following internal equilibrium equations for each shell:

$$\begin{pmatrix} (N_{\alpha\beta} + b_{\alpha\eta}M_{\eta\beta})_{,\beta} - b_{\alpha\eta}N_{\eta\beta}\phi_\beta + \hat{f}_\alpha = 0 \\ M_{\alpha\beta,\beta} + Q_{\alpha 3} = 0 \\ [Q_{\alpha 3} + N_{\alpha\beta}(u_{3,\beta} + b_{\beta\eta}u_\eta)]_{,\alpha} + \hat{f}_3 = 0 \end{pmatrix}_{\mathcal{A}^{(i)}} \tag{18}$$

and the following boundary conditions on the external boundary of each shell:

$$\begin{pmatrix} u_\alpha = 0 \quad \text{or} \quad N_{\alpha\beta} \cdot n_\beta = \hat{F}_\alpha \\ u_{3,\alpha} + b_{\alpha\eta}u_\eta - \gamma_{\alpha 3} = 0 \quad \text{or} \quad M_{\alpha\beta} \cdot n_\beta = \hat{M}_\alpha \\ u_3 = 0 \quad \text{or} \quad [Q_{\alpha 3} + N_{\alpha\beta}(u_{3,\beta} + b_{\beta\eta}u_\eta)] \cdot n_\alpha = \hat{F}_3 \end{pmatrix}_{\partial\mathcal{A}^{(i)}} \tag{19}$$

where n_i is the ith component of the unit vector n normal to delamination front. The displacement is continuous at the delamination edge and, therefore, on Γ, we have

$$\left(\delta U^{(1)} = \delta U^{(2)} = \delta U^{(3)}\right)_\Gamma \tag{20}$$

Hence, for equilibrium, the following conditions have to be satisfied at any point on the delamination edge:

$$\{\mathcal{F}_n(N) = 0, \mathcal{F}_n(M') = 0, \mathcal{F}_n(T) = 0\}_\Gamma \tag{21}$$

where $\mathcal{F}_n(*) = (*)^{(1)} - (*)^{(2)} - (*)^{(3)}$, with $(*)^{(i)}$ corresponding to the value of $(*)$ at the specified point on the delamination boundary of the ith shell; $(M')^{(i)} = M^{(i)} + h^{(i)}N^{(i)}$; and $T_\alpha = Q_{\alpha 3} + N_{\alpha\beta}(u_{3,\beta} + b_{\beta\eta}u_\eta)$ is the effective shear force. It can be noted that these conditions are normally satisfied in a finite element model. Conflict may arise, however, if the delamination edge touches the structural boundary, particularly the boundary with specified displacements where the stresses are expected to develop. Because the delamination generally acts as an imperfection, it is often possible for the base to come in contact with the delaminate after global buckling sets in, and then equilibrium equations (21) may not be valid. Thus, the model can be effectively used for examining the growth of embedded delaminations under postbuckling conditions as long as the delaminated plies do not come in contact with each other.

III. Finite Element Formulation

In this paper, a two-noded curved beam element (BEAM2) (Fig. 2) and the three-noded shell element (SHELL3) (Fig. 3) are used for

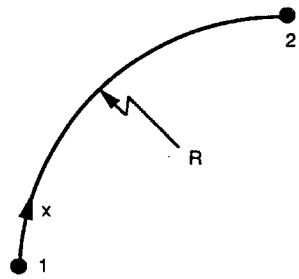

Fig. 2 Two-noded curved beam element (BEAM2).

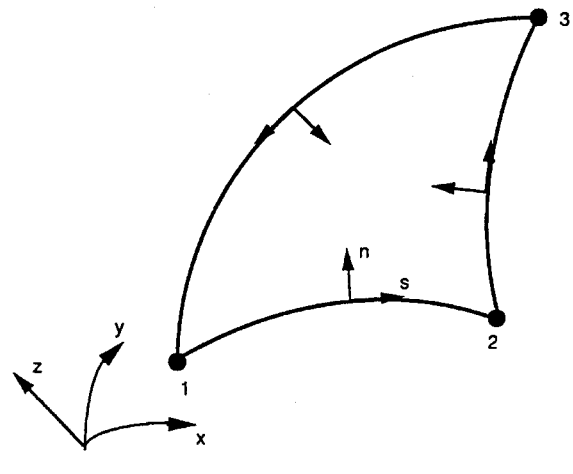

Fig. 3 Three-noded shell element (SHELL3).

modeling stiffened shells. The transverse shear deformation is introduced explicitly in accordance with the Reissner–Mindlin plate theory. Reduced integration is used for the constrained membrane strain energy component to eliminate locking from the elements. The beam degrees of freedom are related to the corresponding shell degrees of freedom in accordance with the Reissner–Mindlin theory of flexure.

A. BEAM2: Two-Noded Curved Beam Element

This element incorporates the following independent degrees of freedom: u, in-plane displacement; w, transverse displacement; $w_{,x}$, slope of midsurface deflection; and γ, transverse shear strain. Thus the element requires C^0 continuous fields for u and γ, and C^1 continuous fields for w. Linear Lagrangian polynomials are used for geometric description x and for the in-plane displacement component u:

$$x = h_1 + h_2\xi \tag{22}$$

$$u = \alpha_1 + \alpha_2\xi \tag{23}$$

and cubic Hermitian polynomials are used for the transverse deflection w:

$$w = \beta_1 + \beta_2\xi + \beta_3\xi^2 + \beta_4\xi^3 \tag{24}$$

where ξ is the natural coordinate and h_i, α_i, and β_i are functions of nodal values x_i, u_i, and w_i, respectively.[5] The field consistency of these shape functions can be demonstrated.[9,10]

B. SHELL3: Three-Noded Triangular Curved Shell Element

This element is described in the curvilinear coordinate system x–y, and the area coordinates are used for field description. Accordingly, we have

$$\{x \quad y \quad 1\} = \sum_{i=1}^{3} L_i \{x \quad y \quad 1\}_i \tag{25}$$

Inverting the preceding relationship, we get

$$L_i = (1/2\Delta)(a_{i1}x + a_{i2}y + a_{i3}) \tag{26}$$

where

$$a_{i1} = y_j - y_k, \qquad a_{i2} = x_k - x_j, \qquad a_{i3} = x_j y_k - x_k y_j$$

$$\Delta = \tfrac{1}{2}(x_2y_3 - x_3y_2 + x_3y_1 - x_1y_3 + x_1y_2 - x_2y_1)$$

and $j = 2, 3, 1, k = 3, 1, 2$ as $i = 1, 2, 3$.

The in-plane displacements and the transverse shear strains need to satisfy C^0 continuity, whereas the transverse deflections need to satisfy C^1 continuity in the present formulation. The independent field variables u, v, w, γ_{xz}, and γ_{yz} are expressed in terms of the nodal degrees of freedom $u_i, v_i, w_i, \varrho_{x_i} \equiv (-w_{,y})_i, \varrho_{y_i} \equiv (w_{,x})_i, \gamma_{xz_i}$, and γ_{yz_i} as

$$\{u \quad v \quad \gamma_{xz} \quad \gamma_{yz}\} = \sum_{i=1}^{3} L_i \{u \quad v \quad \gamma_{xz} \quad \gamma_{yz}\}_i$$

$$w = \sum_{i=1}^{3} \left(N_{1i}w_i + N_{2i}\varrho_{x_i} + N_{3i}\varrho_{y_i}\right) \tag{27}$$

where

$$N_{1i} = L_i + L_i^2L_j + L_i^2L_k - L_iL_j^2 - L_iL_k^2$$

$$N_{2i} = a_{k1}\left(L_i^2L_j + \tfrac{1}{2}L_iL_jL_k\right) + a_{j1}\left(L_i^2L_k + \tfrac{1}{2}L_iL_jL_k\right) \tag{28}$$

$$N_{3i} = a_{k2}\left(L_i^2L_j + \tfrac{1}{2}L_iL_jL_k\right) + a_{j2}\left(L_i^2L_k + \tfrac{1}{2}L_iL_jL_k\right)$$

are the cubic polynomials for the transverse deflection.[11]

In the foregoing element formulations, the interelement C^0 continuity is exactly satisfied for all the field variables. However, the interelement C^1 continuity required for the transverse deflection, in the case of the shell element, is satisfied a posteriori in a weak form using the Hu–Washizu variational principle.[6]

IV. Automated Postbuckling Path Tracing

Automated postbuckling solution involves detection of possible instability in solution and elimination of possible path retracing, classification of the detected instabilities, and computation of the postthrough buckling solution(s).

In the present work, solution instabilities are detected by monitoring the rank of the tangent stiffness matrix. Whenever the determinant of the tangent stiffness matrix changes its sign, the solution senses possible instabilities in that range of load and changes the sign of the next load increment to avoid path retracing. Through a cycle of interactions, locations of instabilities are identified as the load levels for which the tangent stiffness becomes singular. The tangent stiffness is often scaled to minimize numerical errors.[12]

The identified instability points are then classified as limit points or bifurcation points using some simple and cost-effective rules.[7] If the instability point is a limit point, the arc-length continuation is enough to obtain a postbuckling solution path. However, if the instability point happens to be a bifurcation point, the strategies described in detail in Refs. 7 and 8 are used to trace the appropriate postbuckling solution branch.

The nonlinear fundamental state between the two solution points n–1 and n in the neighborhood of the bifurcation point is linearized to obtain the asymptotic solution for obtaining an approximate critical buckling load factor. A linear combination of the normalized eigenvector associated with the critical buckling load factor and its orthogonal counterpart is used to determine the initial postbuckling paths.

V. *J*-Integral Adaptation for Pointwise Energy Release Rate

In this section, the three-dimensional J integral is modified appropriately for representing the energy release rate along the front of an interlaminar delamination crack parallel to the midsurface of a laminated shell.

In the case of delamination, the growth is assumed to be along the interlaminar zone parallel to the midsurface of the shell (i.e., the crack cannot shear into the neighboring laminae). Since the displacement field is made explicitly continuous at the delamination front, the delaminate shell cannot slide or rotate relative to the base shell. Hence, the J integral representing only self-similar crack growth is meaningful in the present case.

The pointwise energy release rate for three-dimensional crack growth (self-similar), $\mathcal{G}(\Gamma)$, is defined as[13]

$$\mathcal{G}(\Gamma)\Delta\Gamma = \lim_{e\to 0} \int_{A_e} \left[W\bar{n}_1 - \bar{\sigma}_{\alpha\beta}\bar{n}_\beta \frac{\partial \bar{U}_\alpha}{\partial \bar{x}_1} \right] \mathrm{d}A$$

$$+ \int_{A_1} \bar{\sigma}_{\alpha 2} \frac{\partial \bar{U}_\alpha}{\partial \bar{x}_1}\,\mathrm{d}A - \int_{A_2} \bar{\sigma}_{\alpha 2} \frac{\partial \bar{U}_\alpha}{\partial \bar{x}_1}\,\mathrm{d}A \tag{29}$$

where $\alpha, \beta = 1, 2, 3$; A_e is the area of the tube of radius e enclosing the crack front, A_1 and A_2 are the areas covering the ends of the tube, and $\bar{n}$, $\bar{\sigma}$, $\bar{U}$, and $\bar{n}$ are defined in the crack tip coordinate system $\bar{x}$ (Fig. 4).

Consider a rectangular tube enclosing the delamination front and passing through the nearest stress recovery points ($S^{(i)}$) of the adjoining elements (Fig. 4). Note that the integrals over the areas A_1 and A_2 nearly cancel each other in a constant strain/stress element model since the quantities like $\bar{\sigma}$ and $\partial \bar{U}_\alpha/\partial \bar{x}_1$ do not vary in the neighborhood of a point in an element domain. Then, Eq. (29) for the self-similar delamination growth becomes

$$\mathcal{G}(\Gamma)\Delta\Gamma = \int_{\Delta\Gamma} \sum_{j=1}^{9} \int_{\Lambda_j} \left(W\bar{n}_1 - \bar{\sigma}_{\alpha\beta}\bar{n}_\beta \frac{\partial \bar{U}_\alpha}{\partial \bar{x}_1} \right) \mathrm{d}\Lambda\,\mathrm{d}\Gamma \tag{30}$$

where Λ_j (j = 1–9) are the segments forming the surface area A_e of the rectangular tube (Fig. 4). Because the Reissner–Mindlin assumptions ($\bar{\sigma}_{13}, \bar{\sigma}_{23}$ are constant over shell thickness, and $\bar{\sigma}_{33} = 0$)

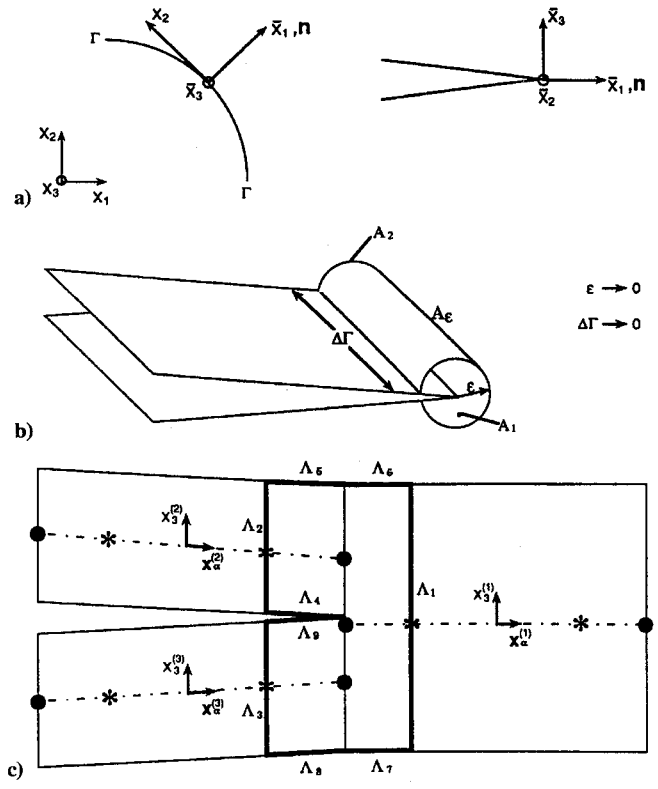

Fig. 4 J integral for delamination growth in a shell model.

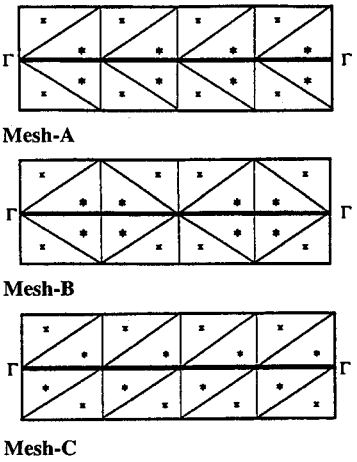

Fig. 5 Finite element mesh and accuracy of energy release rate computation.

are used for the element formulations as well as to achieve displacement continuity at the delamination edge and because $\bar{n} = \{0\ 0\ \pm 1\}$ on the segments Λ_j, $j = 4$–9 (see Fig. 4), the integral in Eq. (30) vanishes over the segments Λ_j, $j = 4$–9. Now, given that $\bar{n} = \{+1\ 0\ 0\}$ on the segments Λ_1 and $\bar{n} = \{-1\ 0\ 0\}$ on the segments Λ_2 and Λ_3, Eq. (30) becomes

$$\mathcal{G}(\Gamma)\Delta\Gamma = \int_{\Delta\Gamma}\left[\int_{\Lambda_1} - \int_{\Lambda_2} - \int_{\Lambda_3}\left(W - \bar{\sigma}_{\alpha 1}\frac{\partial \bar{U}_\alpha}{\partial \bar{x}_1}\right)dx_3\right]d\Gamma \tag{31}$$

Now, carrying out the integration through the thickness for each shell, we get

$$\mathcal{G}(\Gamma)\Delta\Gamma = \int_{\Delta\Gamma} \mathcal{F}_g[\hat{W} - (\bar{N}_{1\alpha}\bar{u}_{\alpha,1} + \bar{M}_{1\alpha}\bar{\theta}_{\alpha,1} + \bar{Q}_{13}\bar{u}_{3,1})]\,d\Gamma \tag{32}$$

Therefore, as $\Delta\Gamma \to 0$, the pointwise energy release rate at any point on the delamination front $\mathcal{G}_g$, computed from the Gauss-point variables, in a finite element model using constant strain elements, is given by

$$\mathcal{G}_g(\Gamma) = \mathcal{F}_g[\hat{W} - (\bar{N}_{1\alpha}\bar{u}_{\alpha,1} + \bar{M}_{1\alpha}\bar{\theta}_{\alpha,1} + \bar{Q}_{13}\bar{u}_{3,1})] \tag{33}$$

where $\mathcal{F}_g(*) = (*)_{g(1)} - (*)_{g(2)} - (*)_{g(3)}$ and $(*)_{g(i)}$ corresponds to the quantities $(*)$ evaluated at specified points on the annular surface. For example, in a finite element analysis, these specified points would be preferably the optimal stress recovery points—normally the Gauss points corresponding to reduced integration[10,14]—in the adjoining element of the ith shell nearest to the delamination front Γ.

A finite element package—NONCAT, or nonlinear computational tool for structural analysis[15]—is developed based on the unified method presented in the earlier sections. The nodal displacements and stresses and strain energy densities at the optimal stress recovery points can be suitably postprocessed to obtain the pointwise energy release rate distribution along the delamination edge. In this paper, the three-noded quasiconforming triangular element is used to model the problem. Incidentally, one has to observe the following precautions while using the finite elements, particularly triangular elements, for the analysis (Fig. 5):

1) The finite element mesh adjoining the delamination edge should be symmetric about the delamination edge such that a) the stress recovery points for all the elements are at the same radial distance from the delamination edge and b) each set of elements from the three shells should have stress recovery points located on a single plane normal to the delamination front. For example, mesh C of Fig. 5 does not have stress recovery points that satisfy either of the two conditions and, hence, cannot be used reliably.

2) One should consider stresses, displacement gradients, and strain energy density only from those adjoining elements that have one of their edges on the delamination edge (type A, represented by $*$ in Fig. 5) since the stresses from the elements with point contact (type B, represented by x in Fig. 5) correspond to a different distance from, and different location on, the delamination edge. Hence, if all the elements are considered for the analysis, the predictions will not be reliable.

In Fig. 5, mesh A is the most accurate and reliable pattern because it satisfies all the foregoing conditions and because the pointwise energy release rates are calculated at equidistant points. Most of these dilemmas vanish, however, if one uses quadrilateral elements.

VI. Numerical Experiments

In this section, we shall consider some numerical examples to validate the model presented in the paper using a simple problem and to demonstrate its applicability to postbuckling analysis of delaminated stiffened composite structures.

A. Model Validation

An isotropic square plate of edge length L with a central elliptic delamination (Fig. 6) is considered for the following numerical experiments. The plate is subjected to biaxial compressive loads, and its boundary is assumed to be clamped against out-of-plane deformations. One-quarter of the plate is modeled for the analysis by imposing appropriate symmetry conditions. For the undelaminate plate, 264 shell elements are used and, for the delaminate and base

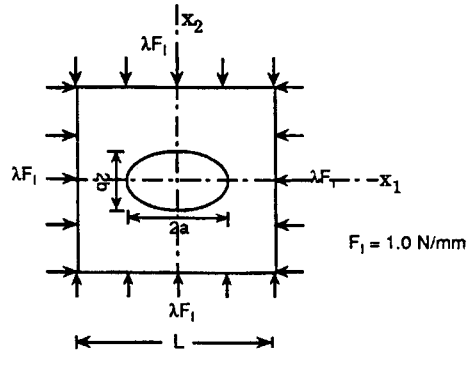

Fig. 6 Square plate with central elliptic delamination.

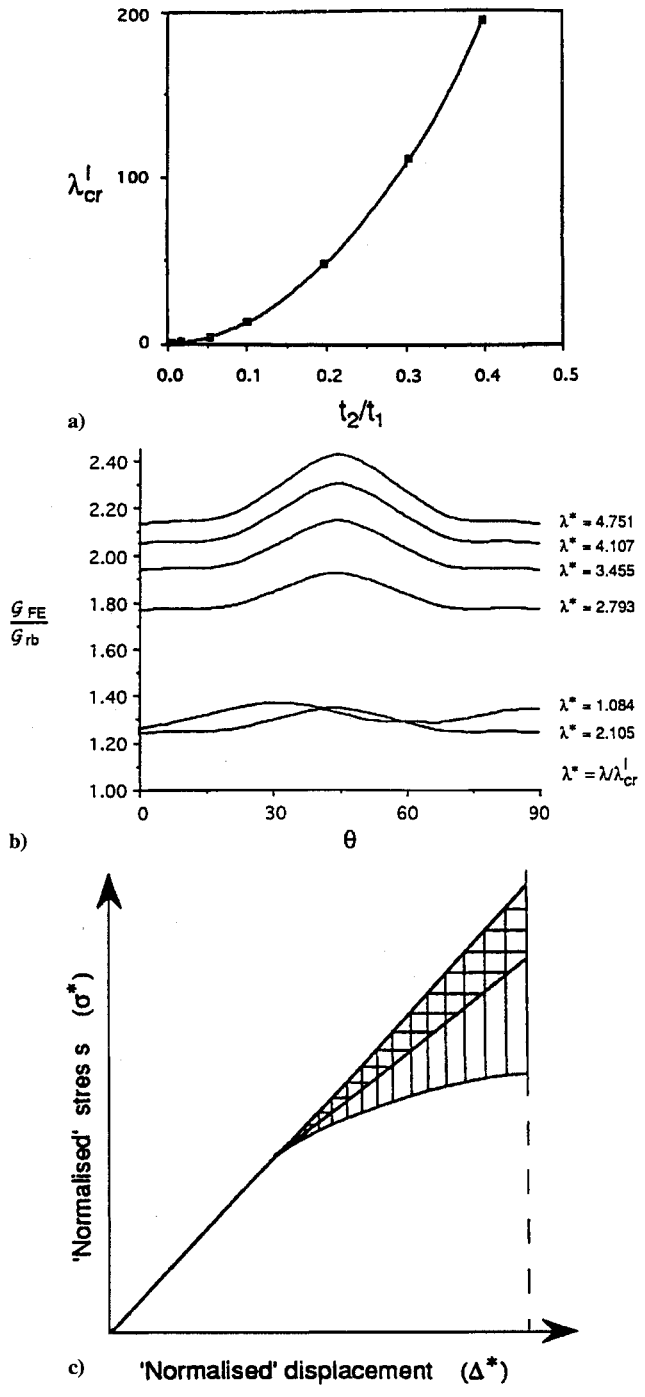

Fig. 7 Clamped square plate with central elliptic delamination (validation of the model): a) critical local buckling strength; comparison of FE solution (—) with analytical solution (■) ($t_2/t_1 = 0.01$, $\lambda^l_{cr} = 0.125$), b) pointwise energy release rate distribution; comparison of FE solution with analytical solution ($t_2/t_1 = 0.01$, $\lambda^l_{cr} = 0.125$), and c) effect of quasi-linear postbuckling; behavior for delaminate on energy release rate; cross-hatched area represents analytical energy release[16]; vertical bars represent actual energy release.

plates, 192 elements each are used. The reference applied biaxial compressive loads are assumed to be of unit intensity ($F_I = 1.0$), and the equilibrium equations are solved at each load step for an applied load $F = \lambda F_I$, where λ is the corresponding load factor (Fig. 6).

The structure is assumed to be isotropic, with Young's modulus $E = 6500$ and Poisson's ratio $\nu = 0.3$. The laminate thickness is chosen as $t_1 = 0.05L$. The numerical experiment is conducted for a near-surface circular delamination with $t_2/t_1 = 0.01$, $a/b = 1.0$, and $a/L = 0.3$. If it is assumed that the base plate and the nondelaminated plates are infinitely stiff when compared to the delaminated plate, the delaminate plate can be considered as a clamped circular plate under the same radial compressive stress.[16] Then the buckling strength of the delaminate plate $[\sigma_c (\equiv \lambda^l_{cr} F_I/t_1)]$ is given by

$$\sigma_c = 1.2233[E/(1-\nu^2)](t_2/a)^2 \tag{34}$$

The local buckling strength of the delaminate plate obtained from the finite element (FE) analysis compares very accurately with the analytical estimate [Eq. (34)] as shown in Fig. 7a.

Further, if it is assumed that the postbuckling deformation is axisymmetric and nearly linear in the neighborhood of the local buckling point, the pointwise energy release rate is given by[14]

$$\mathcal{G}_{rb}(\Gamma) = \frac{(1-\nu^2)t_2}{(1.8285+\nu)E}\left(\sigma_0^2 - \sigma_c^2\right)$$

where $\sigma_0 (\equiv \lambda F_I/t_1)$ is the actual stress level at which the energy release is being computed.

The ratio $\mathcal{G}_{FE}/\mathcal{G}_{rb}$ is plotted along the delamination periphery in Fig. 7b for a case of very thin delaminate configuration ($t_2/t_1 = 0.01$). It can be observed that $\mathcal{G}_{FE}$ is close to $\mathcal{G}_{rb}$ when the postbuckling loads are in the close vicinity of local buckling point (i.e., $\lambda^* \equiv \lambda/\lambda^l_{cr} \simeq 1.0$). However, $\mathcal{G}_{rb}$ is underestimated when compared to $\mathcal{G}_{FE}$, even when $\lambda \simeq \lambda^l_{cr}$. This is because, in the present problem, although the delaminate plate is very thin compared to the total laminate thickness ($t_2/t_1 = 0.01$), the base plate is flexible as opposed to the rigid base as considered in Evans and Hutchinson.[16]

Laminate is also thin when compared to its edge length L ($t_1/L = 0.05$). Hence, the FE model represents a reasonably flexible laminate

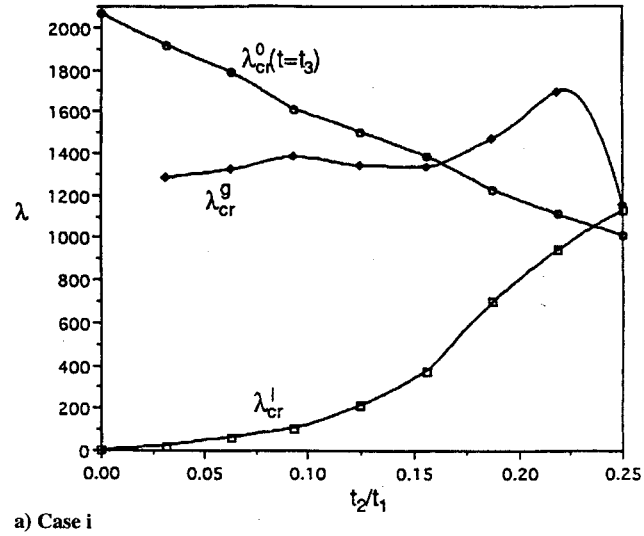

a) Case i

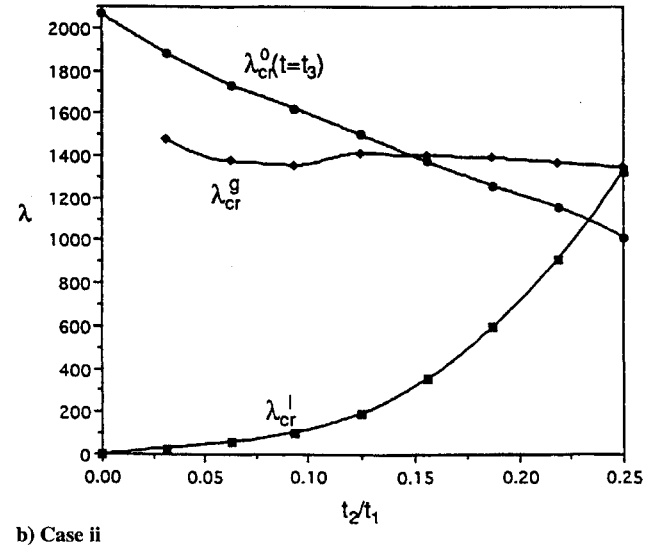

b) Case ii

Fig. 8 Symmetric laminate plate with central elliptic delamination: buckling strength reduction for different delamination thicknesses.

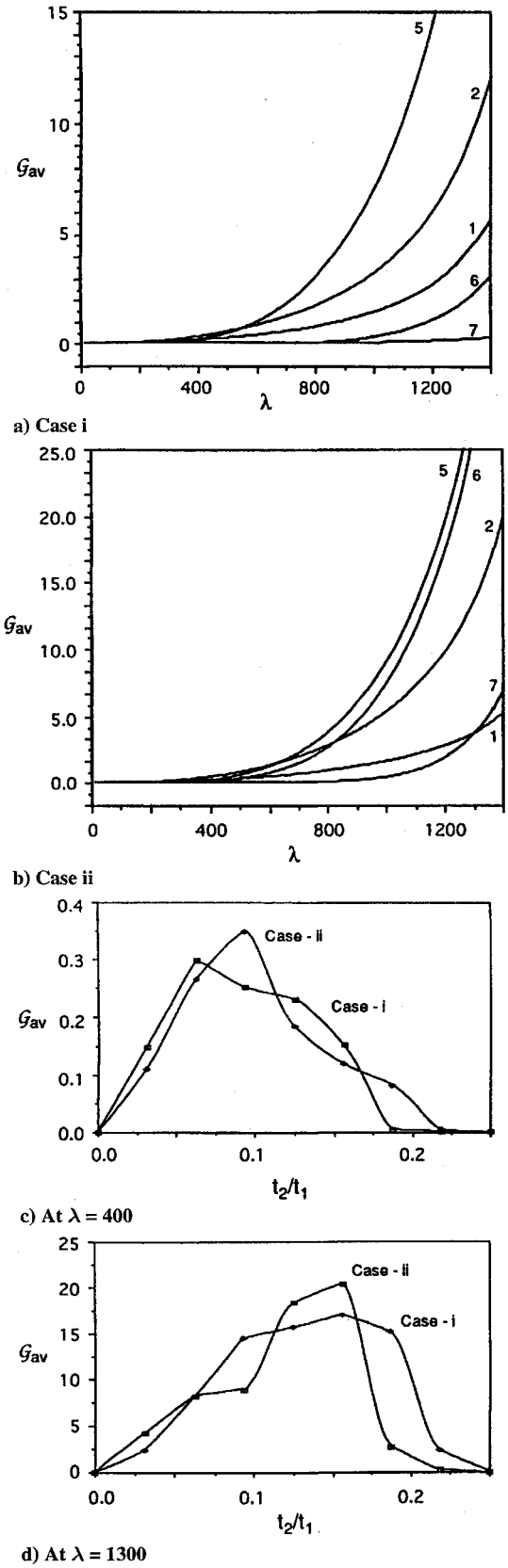

Fig. 9 Symmetric laminate plate with central elliptic delamination: average pointwise energy release rate.

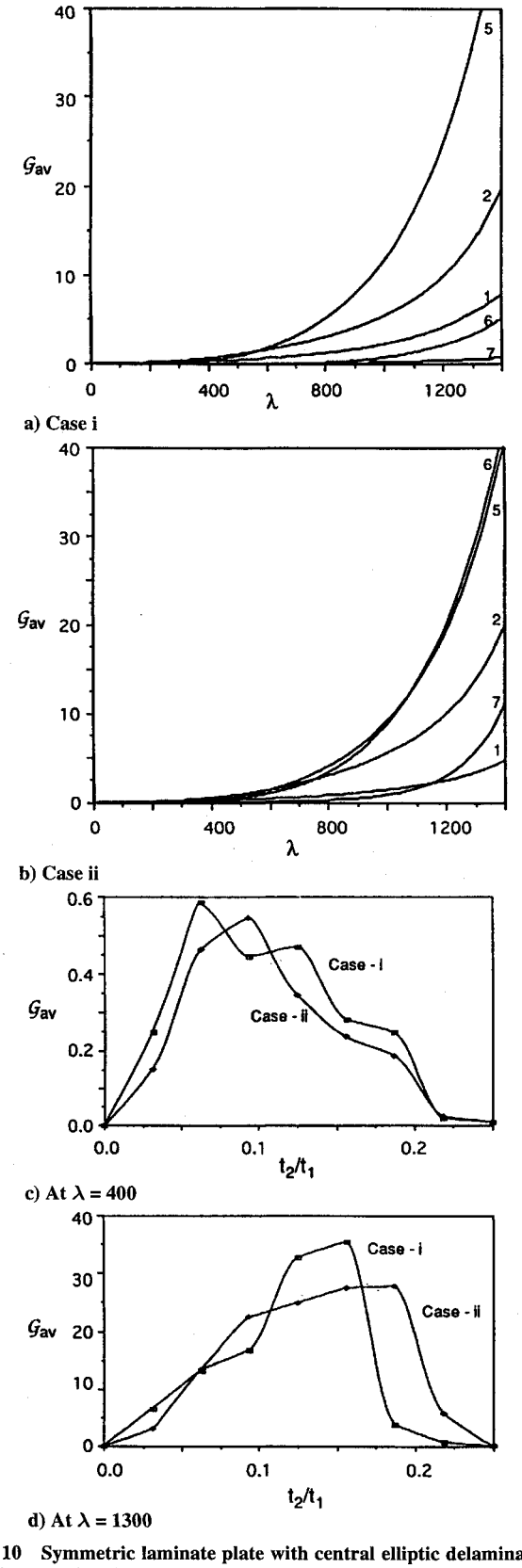

Fig. 10 Symmetric laminate plate with central elliptic delamination: maximum pointwise energy release rate.

and base plates as well. The deviation increases as the buckling load increases beyond its critical value for local buckling of the delaminate plate. This is because the analytical solution [Eq. (35)] is based on the assumption of a quasilinear postbuckling behavior for the delaminate plate. But, in practice, particularly when the laminate is thin, postbuckling behavior of the delaminate plate is highly nonlinear. Accordingly, much higher energy release rates are expected when compared to $\mathcal{G}_{rb}$ as shown in Fig. 7c. Note that, in Fig. 7c, actual stress (σ) and displacement (Δ) are normalized by the critical stress σ_c and the associated critical inward radial displacement Δ_c, respectively.

B. Laminated Plate with Elliptic Delamination

In this section, the plate considered in the previous example is assumed to be symmetrically constituted with 32 orthotropic laminae

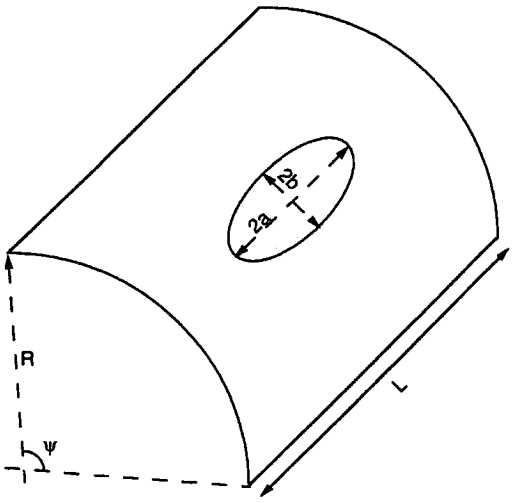

Fig. 11 Laminated cylindrical shell with elliptic delamination.

of equal thickness in the following fashion: i) $(0/90/45/-45)_s$ and ii) $(45/90/-45/0)_s$. The plate thickness is assumed as $t_1 = 0.05L$. The delamination configuration is fixed as $a/L = 0.3$, $a/b = 1.50$, and $t_2/t_1 = 0.10$. The loading and boundary conditions and the FE modeling are the same as in the previous numerical experiments. The material properties for each layer are taken as $E_1 = 208{,}000$, $E_2 = 26{,}000$, $\nu_{12} = \nu_{13} = \nu_{23} = 0.16$, and $G_{12} = G_{13} = G_{23} = 7500$. The delamination is assumed to be between the nth and the $(n+1)$th layer from the top surface, where n takes values from 1 to 15.

The characteristic buckling strengths for the delaminated structure are plotted in Fig. 8 for both cases i and ii. It is found that the local buckling strength becomes nearly equal for $n = 8$ or $t_2/t_1 = 0.25$. The threshold delaminate thickness for which equivalent nondelaminated base plate is stronger than the actual structure in buckling is found to be 0.125 and 0.15 for cases i and ii, respectively. It is interesting to note that the global buckling strength does not vary much with the delaminate thickness for case ii.

The average and maximum energy release rates are plotted for cases i and ii for typical delaminate thickness ($n < 8$) in Figs. 9 and 10, respectively. It should be noted that local buckling does not occur when $n > 8$ and, hence, no delamination growth is expected

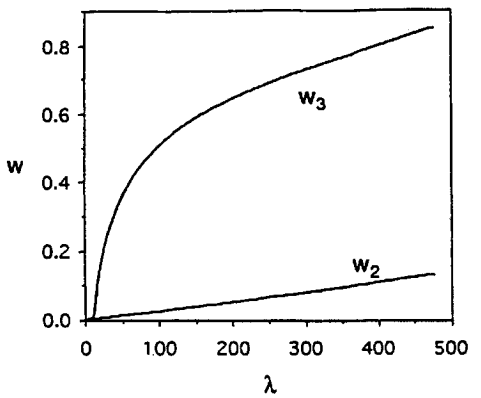

a) ψ = 0 deg

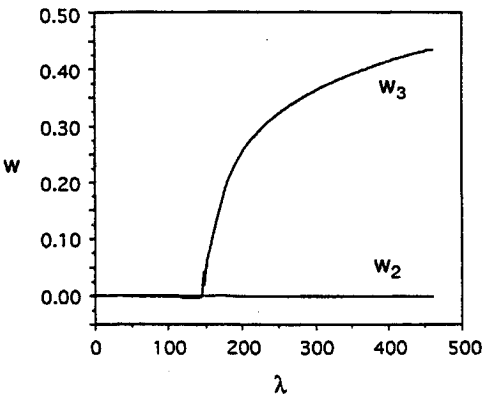

c) ψ = 120 deg

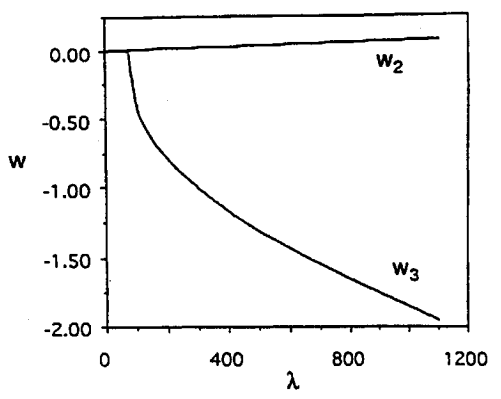

b) ψ = 60 deg

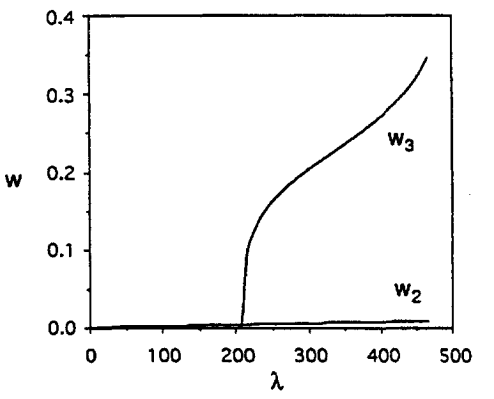

d) ψ = 180 deg

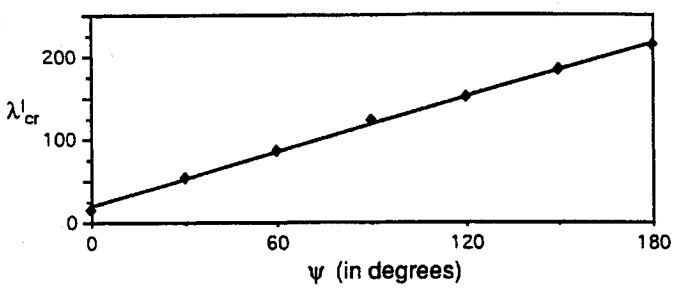

e) Critical local buckling load factor

Fig. 12 Laminated cylindrical shell with elliptic delamination: postbuckling delaminate and base deflections.

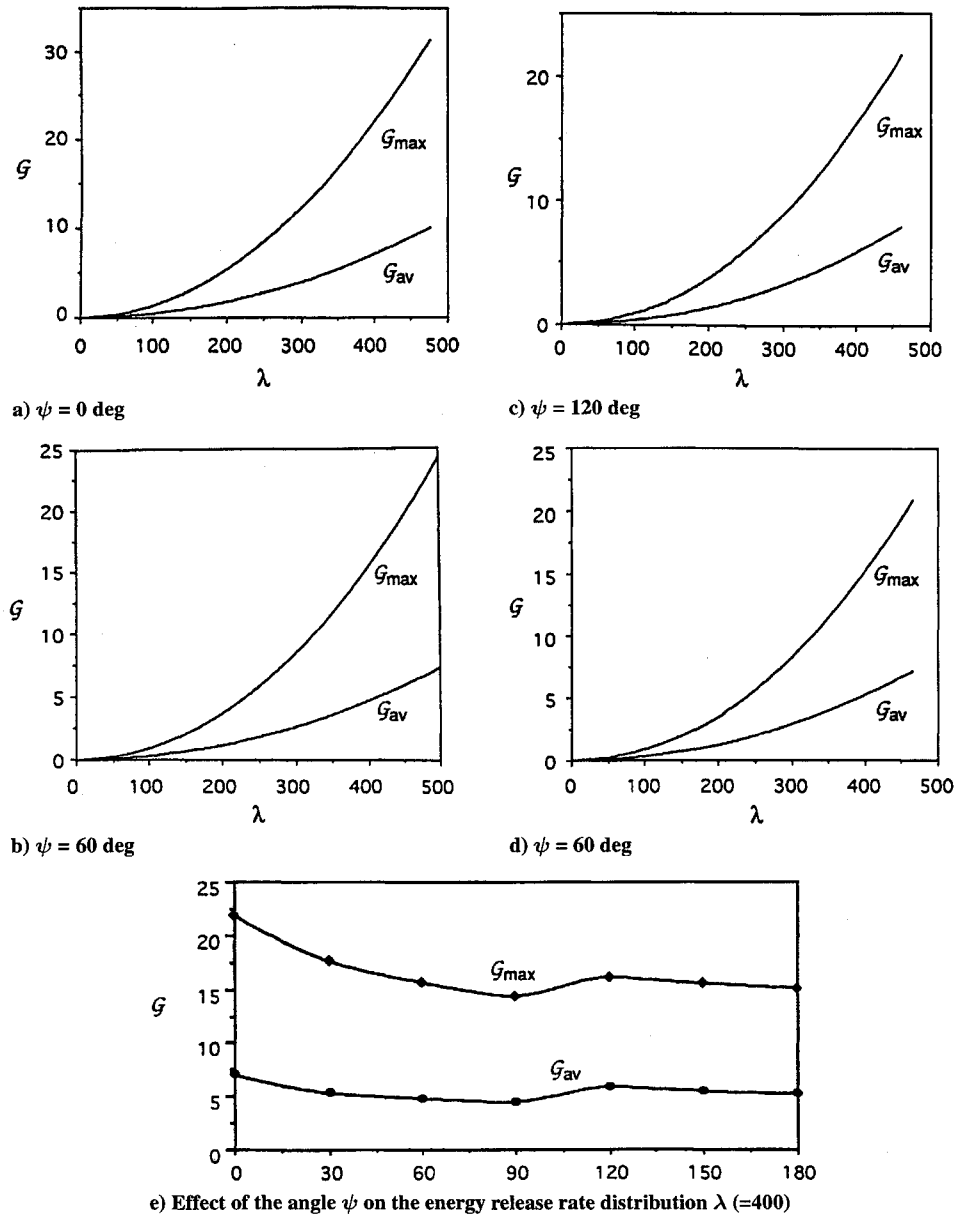

Fig. 13 Laminated cylindrical shell with elliptic delamination: pointwise energy release rate.

because of buckling action. Since the delaminate alternates between symmetric and antisymmetric configurations as n increases, the energy release rate variation also changes for different delaminate thicknesses, as shown in the figures. Variation in the average and maximum energy release rates with the delaminate thickness is plotted for typical load levels in Figs. 9c and 9d and 10c and 10d, respectively. It is observed that the average energy release rate is lower for case i, whereas the maximum energy release rate is lower for case ii.

C. Laminated Shell with Elliptic Delamination

In this section, a cylindrical laminated shell of edge length L with a central elliptic delamination (Fig. 11) under axial compressive loads is considered. The shell is assumed to be constituted with 32 orthotropic laminae of equal thickness stacked in a symmetric fashion: $(0/90/45/-45)_s$. The shell thickness is assumed to be $t_1 = 0.05L$. The delamination configuration is fixed as $a/L = 0.3, a/b = 1.5$, and $t_2/t_1 = 1/32$. The major axis of the delamination is oriented parallel to the shell axis. The material properties for each layer are taken as in the previous example. The reference load intensity is assumed to be unity. The shell boundary is clamped against out-of-plane deformation. Keeping the edge length constant ($R\psi = L$), the shell curvature is changed for the study of its effects on the buckling and delamination growth behavior of the structure.

The postbuckling delaminate and base shell deformation is depicted for typical shell curvatures in Figs. 12a–12d. It can be observed that the critical load factor for local delaminate buckling increases as curvature increases in a linear sense (Fig. 12e). The global buckling strength of the structure also increases as the shell curvature increases; as a result of the presence of the delamination, however, the structure exhibits reduced global buckling strength[17] (results not shown). The maximum and average pointwise energy release rates are presented for varying load factors for typical shell curvatures in Figs. 13a–13d. It can be observed that the energy release rate decreases as the shell curvature increases (Fig. 13e). Thus, the delaminate plate buckling and the delamination growth are delayed in a shell compared to a plate.

D. Stiffened Laminated Plate with Elliptic Delamination

Here we consider a laminated composite square plate of edge length L with 32 orthotropic laminae of equal thickness stacked symmetrically: $(0/90/45/-45)_s$. The plate thickness is assumed to be $t_1 = 0.025L$. The delamination configuration is fixed as $a/L = 0.15, a/b = 1.50$, and $t_2/t_1 = 1/32$. The material properties for each layer are taken as in the previous example. The plate is stiffened in both directions in a symmetric fashion, as shown in Fig. 14. The distance between the stiffeners is assumed to be $d = L/2$. The sectional properties of each stiffener in axial, in-plane flexure,

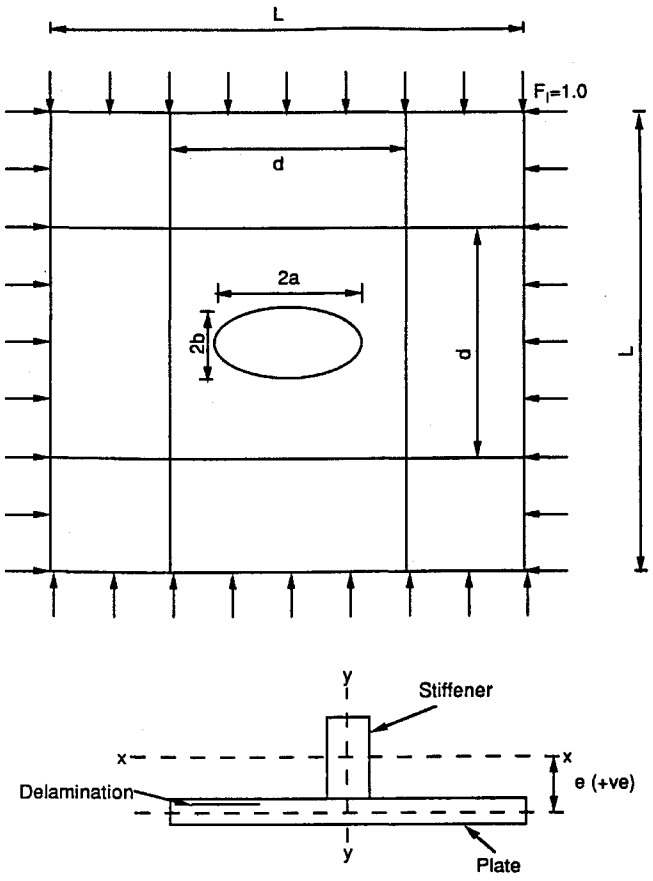

Fig. 14 Stiffened composite plate with elliptic delamination.

out-of-plane flexure, twisting, and transverse shear deformations are, respectively, $EA = 0.104 \times 10^9$, $EI_{xx} = 0.8667 \times 10^9$, $EI_{yy} = 0.2167 \times 10^9$, $GJ = 0.39063 \times 10^7$, and $GA = 0.375 \times 10^6$. The reference applied biaxial compressive loads are assumed to be of unit intensity. The plate boundary is clamped against out-of-plane deformation. Considering the symmetry of the problem, a quarter of the plate is modeled. Twenty beam elements are used to model each stiffener, 92 shell elements each are used to model the delaminate and the base plates, 264 shell elements are used to model the nondelaminated plate between the stiffeners, and 128 shell elements are used to model the rest of the plate. The numerical

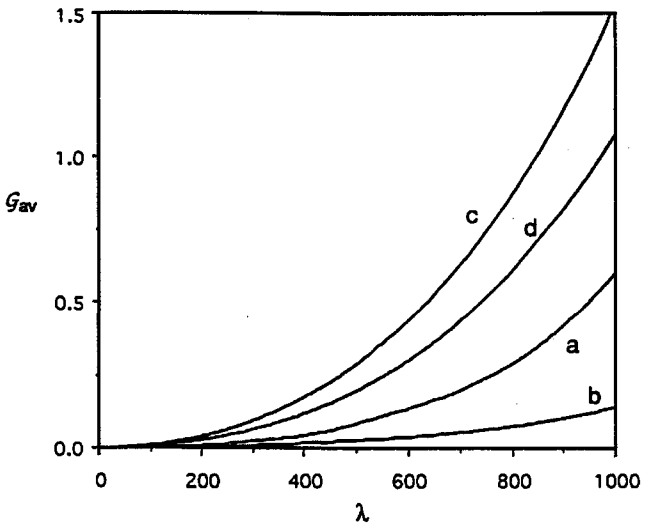

Fig. 16 Stiffened composite plate with elliptic delamination: average energy release rate.

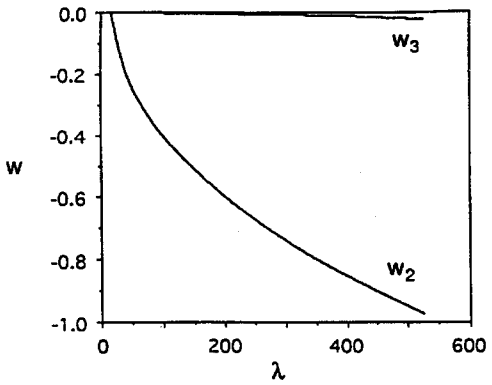

a) No stiffeners, $\lambda^l_{cr} = 24.32$

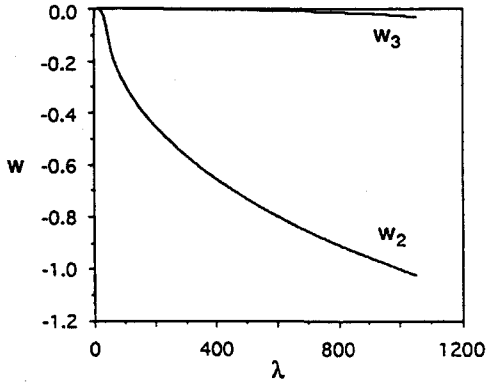

c) Eccentric stiffeners ($e = -10$), $\lambda^l_{cr} = 27.20$

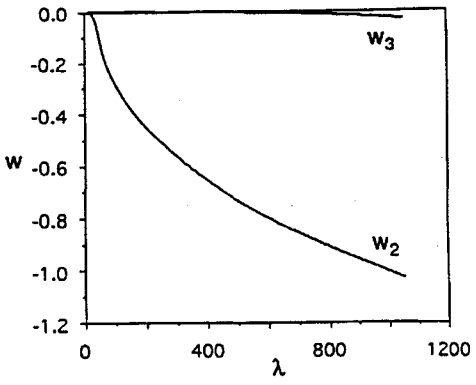

b) Symmetric stiffeners ($e = 0$), $\lambda^l_{cr} = 38.84$

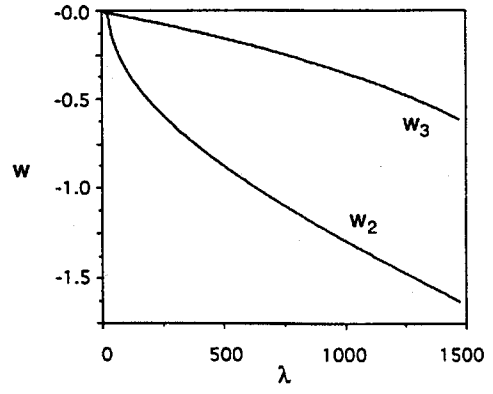

d) Eccentric stiffenres ($e = +10$), $\lambda^l_{cr} = 37.74$

Fig. 15 Stiffened composite plate with elliptic delamination: postbuckling delaminate and base deflections.

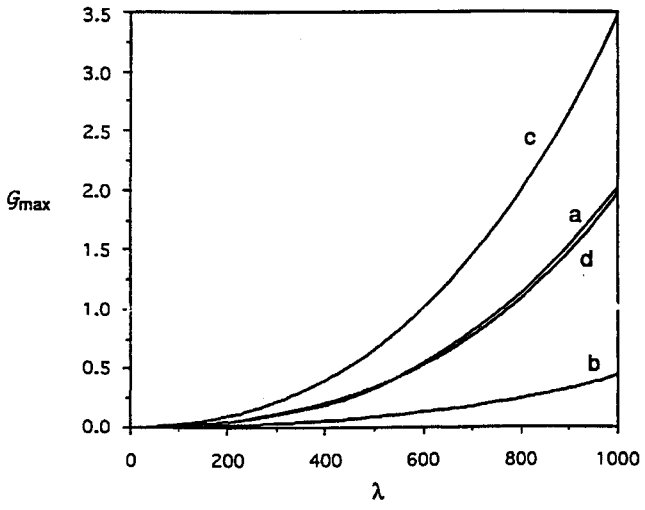

Fig. 17 Stiffened composite plate with elliptic delamination: maximum energy release rate.

experiments are conducted for the plate with no stiffeners and with stiffeners at different eccentricities:

Case a: plate with no stiffeners.

Case b: plate with noneccentric stiffeners, $e = 0$.

Case c: plate with stiffeners on the opposite side of the delamination, $e = -10$,

Case d: plate with stiffeners on the same side of the delamination, $e = +10$.

The postbuckling deformations of the delaminate and base plates are depicted in Fig. 15. The delaminate buckling strength increases with the inclusion of a stiffener. Note that stiffeners with zero eccentricity with reference to the plate provide maximum delay in the delaminate plate buckling. It is interesting to note that stiffeners do not appreciably increase local buckling strength when the delamination is located on the side opposite the stiffeners (case c).

The average and maximum pointwise energy release rates are presented for the different cases in Figs. 16 and 17. It can be observed that noneccentric stiffeners (case b) considerably decrease both the average and the maximum energy release rates for a given load. However, introduction of eccentric stiffeners (cases c and d) lead to appreciable increase in the average energy release rate for a given load. Although stiffeners on the same side as the delamination (case d) slightly decrease the maximum energy release rate, stiffeners on the side opposite the delamination (case c) increase the maximum energy release rate considerably. Thus noneccentric stiffeners (case b) delay the delamination growth appreciably. On the other hand, eccentric stiffeners (cases c and d) may lead to considerably accelerated delamination growth. Thus, from the points of view of both geometric and material failure, noneccentric stiffeners are preferable for reinforcing a delaminated structure. In most aerospace applications, however, the stiffeners are located internally for aerodynamic requirements, and the external surface is highly susceptible to loads causing delaminations. Thus, results for case c appear to be the most critical from practical considerations. Similar behavior was observed with reference to stiffened laminated shells (results not shown).

VII. Concluding Remarks

A unified method has been presented for simple, reliable, and cost-effective modeling and analysis of delaminated, stiffened, laminated composite shells. An error-free, consistent two-noded curved stiffener and three-noded shell elements are derived. The FE are based on elementary curved beam/shallow shell theories. The transverse shear deformation is explicitly introduced in accordance with the first-order shear-deformable beam/plate theories. The C^1 continuity across shell element boundaries is satisfied a posteriori in a weak form using the Hu–Washizu variational principle. Nonlinear stiffness due to large deformation is included for predicting geometrically nonlinear structural behavior. The Newton–Raphson incremental iteration solution strategy is enhanced with arc length–controlled load incrementation and postbuckling branch switching based on a linearized asymptotic solution. Finally, the three-dimensional J integral is used for deriving a simple and reliable method for processing the FE solutions for displacements and stresses to compute pointwise energy release rate distribution along the delamination front. Linear elasticity is assumed throughout. The method presented can effectively model delaminated stiffened composite plates and shells, compute their nonlinear response under general loading and boundary conditions, and compute the energy-release rate distribution at the delamination edge under normal and postbuckling loading environments.

The model presented in this paper is validated by using a simple isotropic plate problem with near-surface circular delamination. Later the method is applied to many general problems of laminated and stiffened composite structures with elliptic delaminations. Some useful observations are made regarding the geometric and material failure in a delaminated stiffened composite structure subjected to compressive loads.

Acknowledgments

This work has been supported by a grant from the U.S. Office of Naval Research, with Y. D. S. Rajapakse as the program official. The first author also acknowledges support by the INDO-U.S. Science and Technology Fellowship under the auspices of U.S. Agency for International Development.

References

[1]Kardomateas, G. A., "The Initial Post-Buckling and Growth Behaviour of Internal Delaminations in Composite Plates," *Journal of Applied Mechanics*, Vol. 60, No. 4, 1993, pp. 903–910.

[2]Kardomateas, G. A., and Pelegri, A. A., "The Stability of Delamination Growth in Compressively Loaded Composite Plates," *International Journal of Fracture*, Vol. 65, 1994, pp. 261–276.

[3]Naganarayana, B. P., and Atluri, S. N., "Energy Release Rate Evaluation for Delamination Growth Prediction in a Multi-Plate Model of a Laminate Composite," *Computational Mechanics*, Vol. 15, No. 5, 1995, pp. 443–459.

[4]Chai, H., Babcock, C. D., and Knauss, W. G., "One-Dimensional Modeling of Failure in Laminated Plates by Delamination Buckling," *International Journal of Solids and Structures*, Vol. 17, No. 11, 1981, pp. 1069–1083.

[5]Naganarayana, B. P., and Prathap, G. P., "Error-Free Field-Consistent Displacement Type Beam Elements for Geometrically Nonlinear Analysis," (to be published).

[6]Huang, B.-Z., Shenoy, V. B., and Atluri, S. N., "A Quasi-Conforming Triangular Laminated Composite Shell Element Based on a Refined First Order Theory," *Computational Mechanics*, Vol. 13, 1994, pp. 295–314.

[7]Huang, B.-Z., and Atluri, S. N., "A Simple Method to Follow Post-Buckling Paths in Finite Element Analysis," *Computers and Structures*, Vol. 57, No. 3, 1995, pp. 477–489.

[8]Naganarayana, B. P., "Incremental Iterative Strategies for Automated Post-Buckling Analysis," *Computers and Structures* (to be published).

[9]Naganarayana, B. P., and Prathap, G. P., "Variational Correctness and Method of Legendre Polynomial Expansion," *Computers and Structures* (to be published).

[10]Naganarayana, B. P., "Consistency and Correctness Principles in Quadratic Displacement Type Finite Elements," Ph.D. Dissertation, Dept. of Aerospace Engineering, Indian Inst. of Science, Bangalore, India, 1991.

[11]Zienciewicz, O. C., *The Finite Element Method*, 3rd ed., McGraw–Hill, New York, pp. 79–101.

[12]Wagner, W., and Wriggers, P., "A Simple Method for the Calculation of Post-Critical Branches," *Computer Methods in Applied Mechanics and Engineering*, Vol. 5, No. 2, 1988, pp. 103–109.

[13]Atluri, S. N., "Energetic Approaches and Path Independent Integrals in Fracture Mechanics," *Computational Methods in Mechanics of Fracture*, edited by S. Atluri, North-Holland, Amsterdam, The Netherlands, 1986.

[14]Barlow, J., "Optimal Stress Locations in Finite Element Models," *International Journal for Numerical Methods in Engineering*, Vol. 10, 1976, pp. 243–251.

[15]Huang, B.-Z., Naganarayana, B. P., and Atluri, S. N., "NONCAT—A NONlinear Computational Analysis Tool for Analysis of Delaminated Composite Structures," Computational Modeling of Aircraft Structures, CMAS Symposium'95, Somerset, NJ, Oct. 1995.

[16]Evans, A. G., and Hutchinson, J. W. "On the Mechanics of Delamination and Spalling in Compressed Film," *International Journal of Solids and Structures*, Vol. 20, No. 5, 1984, pp. 455–466.

[17]Naganarayana, B. P., and Atluri, S. N., "Strength Reduction and Delamination Growth in Thin and Thick Composite Plates Under Compressive Loading," *Computational Mechanics*, Vol. 16, No. 3, 1995, pp. 170–189.